Metal-oxide based microjets for the simultaneous removal of organic pollutants and heavy metals

Katherine Villa†, Jemish Parmar[£]†, Diana Vilela[£]†, Samuel Sánchez†, §*

† Institute for Bioengineering of Catalonia (IBEC), The Barcelona Institute of Science and Technology, Baldiri Reixac 10-12, 08028 Barcelona Spain

§ Institució Catalana de Recerca i Estudis Avancats (ICREA), Pg. Lluís Companys 23, 08010, Barcelona, Spain

ABSTRACT

Water contamination from industrial and anthropogenic activities is nowadays a major issue in many countries worldwide. To address this problem, efficient water treatment technologies are required. Recent efforts have focused on the development of self-propelled micromotors that provide enhanced micro-mixing and mass-transfer by the transportation of reactive species, resulting in higher decontamination rates. However, a real application of these micromotors is still limited due to the high cost associated to their fabrication process. Here, we present Fe_2O_3-decorated SiO_2/MnO_2 microjets for the simultaneous removal of industrial organic pollutants and heavy metals present in wastewater. These microjets were synthezised by low-cost and scalable methods. They exhibit an average speed of 485±32 μm s^{-1} (~28 body length s^{-1}) at 7% H_2O_2, which is the highest reported for MnO_2-based tubular micromotors. Furthermore, the photocatalytic and adsorbent properties of the microjets enable the efficient degradation of organic pollutants such as

tetracycline and rhodamine B under visible light irradiation, as well as the removal of heavy metal ions such as Cd^{2+} and Pb^{2+}.

KEYWORDS: micromotors; photocatalytic; water purification; Fenton; magnetic control; iron oxide; manganese oxide.

1. INTRODUCTION

Considerable research efforts are underway to develop highly efficient water treatment technologies that can mitigate water scarcity for millions of people.[1,2] These include using nanotechnology and nanomaterial-based methods to rapidly improve the water cleaning process due to their high specific surface area and excellent intrinsic properties.[3,4] Recently, self-propelled nano/micromotors have reported to speed up the removal of a wide variety of pollutants from water due to the enhanced mixing of the fluid around them.[5–9] Thus, micromotors have been employed for the removal of organic pollutants,[10–12] heavy metals,[13,14] bacterial contamination[15,16] and biological warfare agents.[17] Commonly, catalytic micro- and nanomotors use a fuel source such as hydrogen peroxide (H_2O_2) for self-propulsion, converting chemical energy into kinetic energy by decomposing the fuel catalyzed by precious metals such as platinum, silver or iridium.[18–22]

Tubular micro- and nanomotors are usually fabricated by polycarbonate-template-assisted electrodeposition,[23] self-assembly of organic molecules[24,25] and rolled-up nanotechnologies.[26] These methods lead to micro- and nanomotors with a precise geometry and controlled shape. However, specialized equipment such as metal evaporators, cleanroom facilities for lithography process or electrochemical workstations is required to use these technologies.[27,28] Therefore, there is a need for the development of facile synthesis of micro- and nanomotors that involves only basic

and inexpensive equipment.[29] Some efforts have been made to develop other simple methodologies for the synthesis of micro- and nanomotors, by using emulsions,[30] microfluidics[31,32] or by simple aggregation processes,[33] but tubular motors cannot be obtained easily by such procedures. Our group has recently reported the fabrication of tubular mesoporous silica micromotors by sol-gel synthesis using a polycarbonate membrane as a template, which uses platinum as catalyst for the self-propulsion in H_2O_2.[34] In order to reduce the cost associated with large-scale micromotors synthesis and solve platinum poisoning under harsh chemical environments, micromotors based on metal oxide catalysts have previously been proposed as inexpensive materials for the propulsion of micromotors, but the resulting speeds are still too low.[30,33,35–38]

Previous research has demonstrated the potential of combining the self-propulsion of micromotors with advanced oxidation processes (AOPs) such as Fenton[11,39] reactions and photocatalysis[17,40,41] for environmental remediation. Photocatalytic processes are environmentally-friendly and offer the possibility of using solar radiation as the main energy source, which significantly decreases the cost of water treatments[2,42–44]. Considering that the visible region is one of the major components of solar irradiation, the development of photocatalytic and Fenton-like micromotors that can harvest solar irradiation to remove different kind of pollutants has the potential to advance micromotors-based water cleaning methods.

Here, we present multifunctional mesoporous silica-based microjets with MnO_2 immobilized on the inner surface and decorated with γ-Fe_2O_3 nanoparticles (NPs) (band gap of ~2.0 eV)[45] as magnetic photocatalyst on the outer surface, hereafter called $FeSiMnO_x$ microjets (Fe_2O_3/SiO_2-MnO_2 microjets). $FeSiMnO_x$ microjets are fabricated by growing silica tubes on a polycarbonate template by sol-gel method. The immobilized MnO_2 and Fe_2O_3 catalysts act as functional materials for both propulsion and removal of pollutants. Furthermore, the $FeSiMnO_x$ microjets are

magnetically steered and guided in a controlled manner, facilitating their recovery and further reuse.

2. EXPERIMENTAL SECTION

2.1. Synthesis of microjets

Mesoporous silica (SiO_2) microtubes were obtained using a polycarbonate membrane (Whatman, conical-shaped micropores with 2 µm diameter) as the template, and a mixture of tetraethyl orthosilicate (TEOS, ≥99.0% (GC), Sigma-Aldrich), hexadecyltrimethylammonium bromide (CTAB, BioUltra ≥99.0%, Sigma-Aldrich), 3-aminopropyltriethoxysilane (APTES, 99.0%, Sigma-Aldrich) and triethanolamine (TEOA, ≥99.0 %, Sigma-Aldrich), as described in a previous work reported by our group.[34] These SiO_2 microtubes were used as the scaffold for the micromotors. Once the mesoporous silica tubes were grown inside the membrane, it was placed in 30 mL of 10mM $KMnO_4$ (ACS reagent ≥99.0%, Sigma-Aldrich) and transferred into a 50 mL Teflon-lined stainless-steel autoclave and heated at 160 °C for 9 h. Afterwards, the black resulting membrane was polished with water to remove the excess of MnO_2. The SiO_2-MnO_2 microtubes were released by dissolving the membrane template in CH_2Cl_2 (GPR RECTAPUR, VWR) for 15 min and then washing them twice for 3 min with CH_2Cl_2, ethanol and water, respectively.

To optimize the MnO_2 filling inside the silica tubes, different $KMnO_4$ loadings of 10, 20 and 30 mM were tested. The best swimming behavior was observed in MnO_2-based microtubes synthesized with 10 mM of $KMnO_4$, thus being this concentration of $KMnO_4$ selected as the optimal concentration for our fabrication protocol.

Finally, the surface of SiO_2-MnO_2 microtubes was functionalized with γ-Fe_2O_3 (Maghemite, nanopowder <50 nm, Sigma-Aldrich) by mixing them with 1 mL of an ethanolic suspension containing 0.001 g of γ-Fe_2O_3 nanoparticles (NPs) for 6 h. After this, the Fe_2O_3/SiO_2-MnO_2 microtubes were separated from the NPs by filtering the suspension with a 2 μm pore size membrane (Whatman), and then they were washed several times with ethanol and water, respectively.

For the sake of simplicity, the Fe_2O_3/SiO_2-MnO_2-based microtubes have been labelled as $FeSiMnO_x$ microjets, $SiMnO_x$ microjets (without Fe_2O_3) or $FeSiO_x$ microtubes (without MnO_2).

2.2. Microjets characterization

A JEOL JEM-2100 LaB6 microscope operating at 200 kV accelerating voltage and equipped with an Oxford Instruments INCA x-sight (Si(Li) detector) and a Zeiss SESAM microscope (200kV) equipped with an EDS System from ThermoFisher were used to perform transmission electron microscopy (TEM) and Energy-dispersive X-ray (EDX) analysis. Scaning Electron Microscopy (SEM) images were taken on a FEI NOVA NanoSEM 230 microscope. Surface charge of γ-Fe_2O_3 NPs was examined by Dynamic Light Scattering (DLS, Wyatt Möbius coupled with an Atlas cell pressurization system). The motion of microjets was observed and recorded by using an inverted optical Microscope (Leica DMI 3000 B) equipped with a camera (Leica DFC 3000 G) with LAS V4.5 software. For recording of the videos, 10 μl of microjets suspension was placed onto a glass slide and 0.2 wt% of sodium dodecyl sulfate (SDS, ACS reagent ≥99.0%, Sigma-Aldrich) was added in the presence of different concentrations of H_2O_2. The speed and tracking of microjets was calculated from the recorded videos and analyzed using openCV libraries and Python-based software.

The magnetic control setup consists of two pairs of coils in Helmholtz configuration, which create a magnetic field gradient in, respectively, the X and Y directions. Cylindrical steel rods are put inside the coils to increase the strength field. The intensity of the gradient is controlled remotely through an Arduino microcontroller, whose current is amplified using a TS250 Wave Amplifier. A Python script with an user interface is used to send orders to the Arduino in real time, allowing total control of the magnetic field from a PC. The gradient per unit of electric current created by the coils for each pair is 18 G $(A \cdot mm)^{-1}$. During the magnetic control experiments, a maximum current of 2.5 A was used.

2.3 Photocatalytic set-up

The photocatalytic degradation of aqueous solutions of rhodamine (RB) and tetracycline (TC) was carried out in a 5 mL cylindrical glass vessel. For the photocatalytic experiments, a 300 W high pressure UV-visible lamp (Ultravitalux Osram, 280-780 nm) was used as light source. A polyester UV filter sheet (Edmund Optics) was used to remove wavelengths radiation below 400 nm and to ensure only visible irradiation. In all degradation experiments, 1 mL of RB (10 ppm) or TC (50 ppm) solution containing 0.3 mg of microjets was placed in the vessel with 0.2 wt% SDS as surfactant. No acidic or basic pH adjustments were performed during the photocatalytic tests.

Prior to illumination, the microjets were kept in the dark for 30 min to reach adsorption-desorption equilibrium on their surface. In this way, the decrease in the absorbance signal of the pollutants due to adsorption can be ruled out in the degradation experiments. After that, the lamp was turned on and 5 wt% H_2O_2 was added to initiate the reaction. Liquid aliquots were periodically taken out during the reaction (before the absorbance measurements, the solids were removed by centrifugation in the case of $SiMnO_x$ microjets or by a magnet in the case of $FeSiMnO_x$ and $FeSiO_x$

microjets). They were then immediately analyzed by measuring their absorbance at 555 nm and 358 nm for RB and TC respectively, using a UV-Vis spectrophotometer (Specord 50 plus).

Control experiments without microjets (only H_2O_2 or H_2O_2 + light irradiation) were also performed to evaluate the contribution of the photolysis of H_2O_2 on the oxidation of our target pollutants. Additionally, a test with non-filled $FeSiO_x$ microtubes (without MnO_2) in the presence of H_2O_2 under light irradiation was also carried out to investigate the influence of the motion of microjets on the resulting photocatalytic performance.

2.4 Heavy metals removal

In order to prove the capability of $FeSiMnO_x$ microjets to capture heavy metals, 0.3 mg of the microjets was added to 1 mL of a water solution, which contained 1 ppm of lead (Pb^{2+}) and cadmium (Cd^{2+}), in the presence of another contaminant (10 ppm of RB). After allowing the $FeSiMnO_x$ microjets to swim for 7 and 15 min in the previously prepared solution, the concentration of both heavy metals was determined at both time intervals by square wave voltammetry using a mercury-coated glassy carbon electrode (GCE)[46] as working electrode. Prior to the measurements, any trace of H_2O_2 was removed by adding an excess of 1 M sodium bisulfite solution to avoid any interference in the electrochemical signals. First, the mercury film was pre-plated at the beginning from a non-deaerated 80 mg L^{-1} mercury solution (in 0.02 M HCl), by holding the carbon strip electrode at −1.15 V for 15 min. Then, the potential was switched to −0.20 V for a 2 min cleaning period. The subsequent cycles involved the Pb^{2+} and Cd^{2+} deposition (3 min of preconcentration at −1.15 V) and stripping steps (from -1.15V to -0.2V). Before the next measurement, the electrode is maintained for 60 s at -0.2 V to ensure that Pb and Cd do not remain on the working electrode surface. After finishing the measurement of heavy metals, the mercury

film is removed from the GCE by holding it at +0.4 V for 5 min. An acetate buffer 0.02 M solution (pH 4.8) was used as electrolyte during the sensing of the heavy metals, the intermediate steps and the removal of the mercury film from the GCE.

The linear range was between 0.01–0.1 ppm for Pb^{2+} ($Area_{peak}$=1.086+0.027[Pb^{2+}], r=0.980) and Cd^{2+} ($Area_{peak}$=0.04255+0.01405[Cd^{2+}], r=0.990), respectively. To measure the concentration of Pb^{2+} and Cd^{2+} ions from the assay solution, a dilution 1:10 (total volume 5 mL, 0.02 acetate buffer solution) was carried out, before and after the removal of both ions by the $FeSiMnO_x$ microjets.

3. RESULTS AND DISCUSSION

$FeSiMnO_x$ microjets were synthesized by facile and scalable procedures as shown in **Figure 1**. The tubular structure was achieved by using a polycarbonate (PC) membrane as template and a mixture of SiO_2 precursors at 80 ºC.[34] Then, 10 mM $KMnO_4$ was reduced to MnO_2 inside the pores of the membrane by a hydrothermal reaction. After releasing the tubes from the PC membrane, γ-Fe_2O_3 NPs were mixed with SiO_2-MnO_2-based microtubes and attached to their outer surface. The final tubular structure consists of a biconical mesoporous silica tube with MnO_2 inner layer and γ-Fe_2O_3 NPs on the outer surface (**Figure 1**).

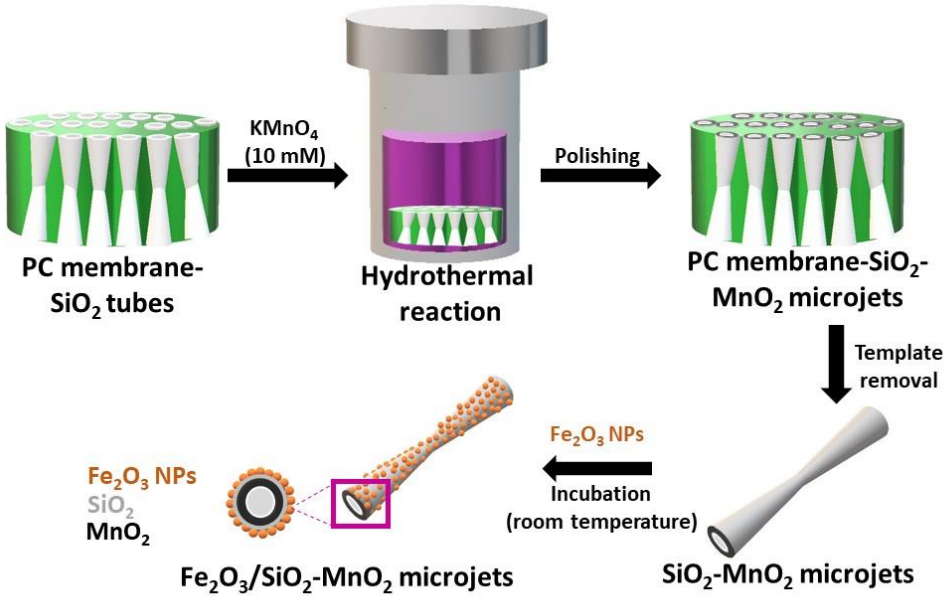

Figure 1. Chemical fabrication of mesoporous Fe_2O_3/SiO_2-MnO_2 ($FeSiMnO_x$) microjets for the photocatalytic degradation of organic pollutants and removal of heavy metals.

The structural and morphological characterization of the microjets was carried out by TEM-EDX-mapping and SEM, respectively (**Figure 2**). The SEM images show that the microjets have a tubular biconical structure (see blue inset) with a length of about 17 µm (**Figure 2A**). The length of the microjet is co-related with the thickness of the PC membrane (20 µm) used for the synthesis process. The TEM image in **Figure 2B** shows a color contrast along the $SiMnO_x$ tube due to the non-homogeneous dispersion of MnO_2 on the inner surface (as evidenced by the TEM mapping of several tubes, see SI **Figure S1)**. This heterogeneity in the inner surface of the microjets may result in several nucleation points for bubble growth, which can be beneficial for the microjets motion. After the modification of the outer surface of the $SiMnO_x$ microjets with γ-Fe_2O_3 NPs, it is observed that the γ-Fe_2O_3 NPs are distributed along the surface (**Figure 2C** and red dotted inset) and on the edges of the cavity of the $FeSiMnO_x$ microjets (see blue square inset in **Figure 2C**). **Figure 2D** displays the rough outer surface of the $FeSiMnO_x$ microjets. This results from the

adherence of γ-Fe_2O_3 NPs to the silica surface, due to the electrostatic interaction between the external -NH_2 groups from the SiO_2 tubes surface and the negative charge of γ-Fe_2O_3 NPs (-7.43 ± 1.53 mV, average ± standard error of mean, n = 6) measured by DLS. As observed in **Figure 2E**, these γ-Fe_2O_3 NPs have a diameter size ranging from 20-50 nm. The TEM-EDX spectrum confirms the presence of Si, Fe and Mn in $FeSiMnO_x$ microjets (**Figure 2F**). Furthermore, EDX mapping and the profile analysis of the tubes for the different elements show the distribution of Mn in the tubes and the dispersion of Fe_2O_3 NPs along their surface (**Figure 2G and 2H**).

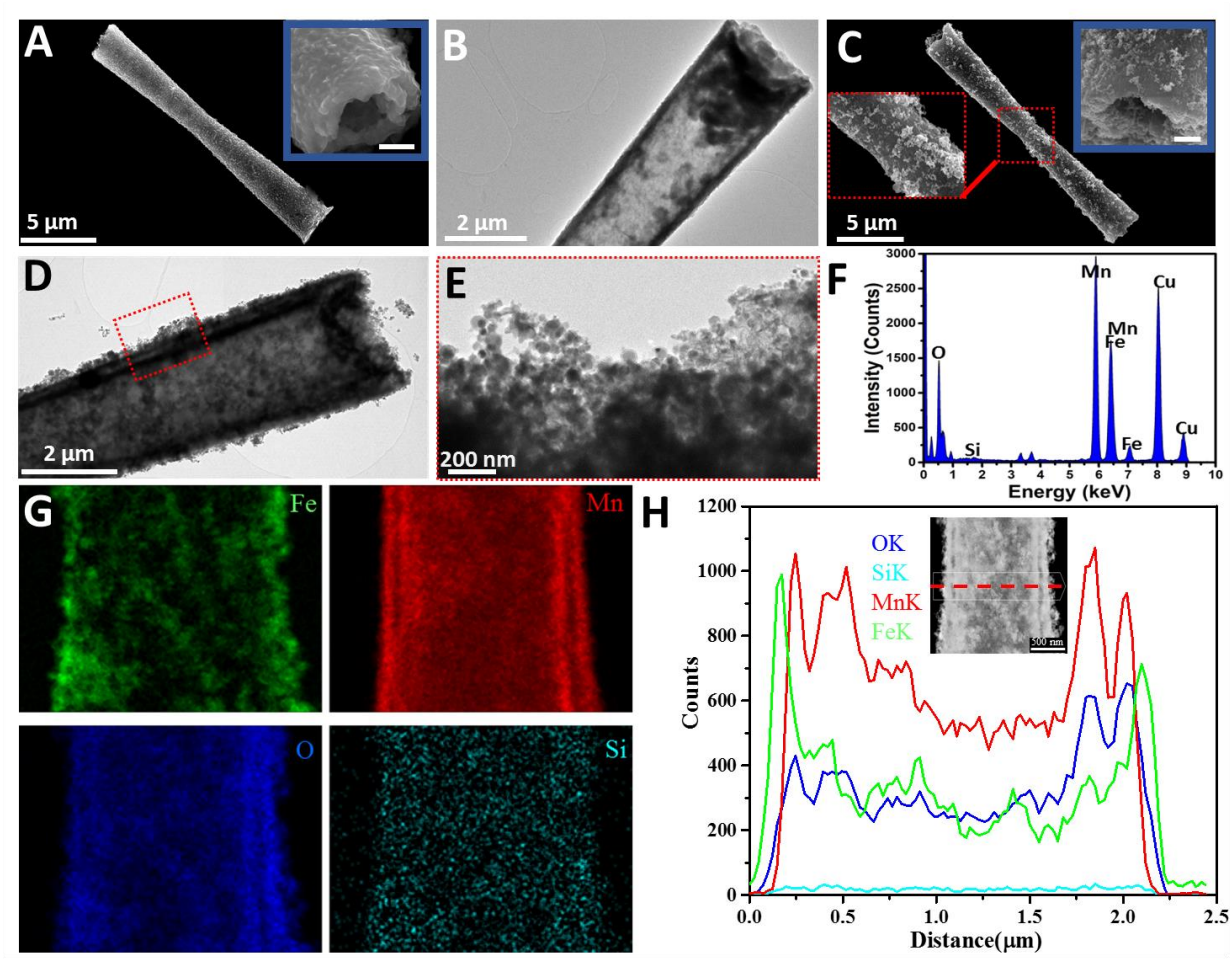

Figure 2. Characterization of $FeSiMnO_x$ microjets. A) SEM image of the $SiMnO_x$ microjet, inset

corresponding to the cavity of the tube, B) TEM image of the $SiMnO_x$ microjet, C) SEM image of the $FeSiMnO_x$ microjet, blue solid inset corresponding to the tube cavity and red dotted inset corresponding to γ-Fe_2O_3 NPs on the outer surface, D) TEM image of the $FeSiMnO_x$ microjet, E) Magnification of the red dotted lines in Figure 2D, F) EDX spectrum of the $FeSiMnO_x$ microjet, G) EDX mapping of the $FeSiMnO_x$ microjet and H) element profile of the $FeSiMnO_x$ (represented by a red dotted line).

The mechanism of propulsion of $FeSiMnO_x$ microjets is based on the catalytic descomposition of H_2O_2 into water and oxygen gas by MnO_2, leading to the generation of microbubbles in their cavity. The motion capabilities of $FeSiMnO_x$ and $SiMnO_x$ microjets were examined using an optical microscope. To find out the relation between MnO_2 loading and motion of $SiMnO_x$ microjets, different concentrations of $KMnO_4$ (10-30 mM) were studied. As shown in **Figure S2**, an increase of $KMnO_4$ concentration (>10 mM) resulted in a total blockage of the internal holes of the microjets (**Figure S2B-C**) and/or rupture of the tubular structure in half (**Figure S2C**). As a result, not all the microtubes were swimming (**Video S1**), and if they were their speed was very low (**Video S2**). Therefore, 10 mM $KMnO_4$ was selected as the optimal concentration for the synthesis of $SiMnO_x$ and $FeSiMnO_x$ microjets.

Figure 3A shows the motion behavior of $SiMnO_x$ and $FeSiMnO_x$ microjets in 5 wt% H_2O_2 and 0.2 wt% of SDS (**Video S3** and **S4**, respectively). Both microjets display directional trajectories, but $FeSiMnO_x$ microjets show a faster speed than $SiMnO_x$. This improvement in the speed of $FeSiMnO_x$ microjets is related to the presence of γ-Fe_2O_3 NPs, which can also catalyze the decomposition of H_2O_2 into O_2 gas through a series of complex reactions.[47–49] Recently, we found that free iron-based NPs do not exhibit bubble propulsion in the presence of H_2O_2, but once they become a cluster they can self-propel by releasing bubbles from the cavities of the cluster and the

rough surface.[33] Therefore, the agglomeration of γ-Fe_2O_3 NPs on the tubes surface might be beneficial for the enhancement of the propulsion of $FeSiMnO_x$ microjets.

Figure 3B illustrates the speed of $SiMnO_x$ and $FeSiMnO_x$ microjets at different H_2O_2 concentrations (1, 3, 5 and 7 wt%). The speed of the jets increases by increasing the fuel concentration, reaching the highest values at 7 wt% H_2O_2 of 165±13 μm s^{-1} and 485±32 μm s^{-1} for $SiMnO_x$ and $FeSiMnO_x$ microjets respectively. $FeSiMnO_x$ microjets are almost 3 times faster than the bare $SiMnO_x$, swimming at approximately 28 body length s^{-1} at 7 wt% H_2O_2. As despicted in **Table 1**, the speed showed by $FeSiMnO_x$ microjets is the highest reported so far for tubular micromotors propelled by non-metallic catalysts. The trajectories of the $SiMnO_x$ and $FeSiMnO_x$ microjets are shown in **Figure 3C**. It was observed that $FeSiMnO_x$ and $SiMnO_x$ microjets move randomly following helical or straight paths.

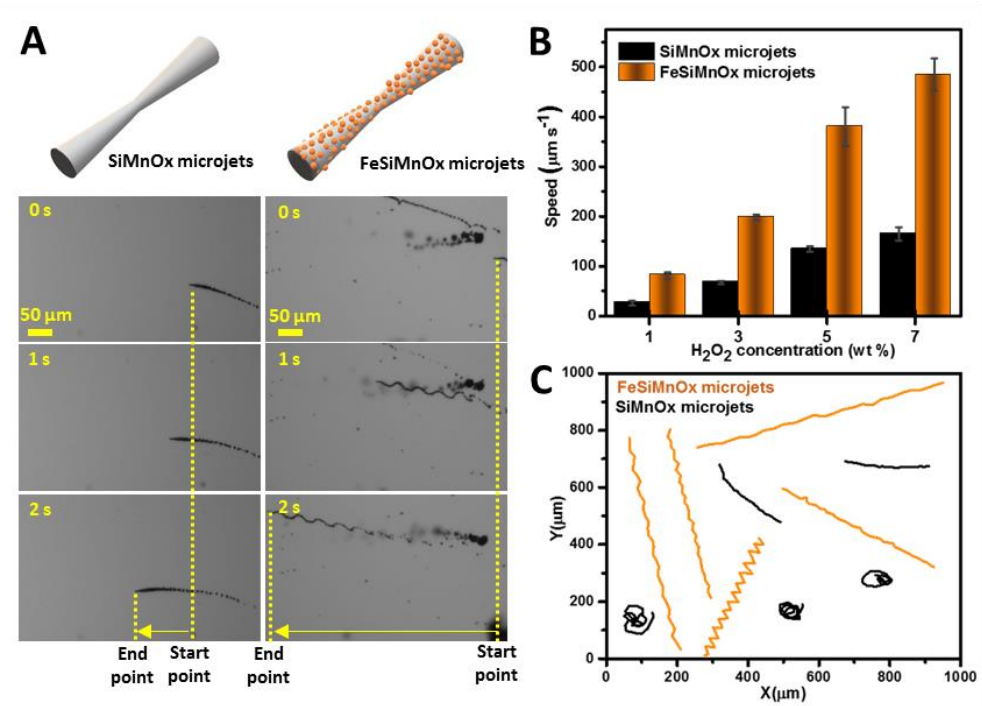

Figure 3. Motion characterization of $FeSiMnO_x$ microjets. A) Optical images of the trajectories of $SiMnO_x$ and $FeSiMnO_x$ microjets swimming for 2 s at 5 wt% H_2O_2, B) speed of the $SiMnO_x$ and $FeSiMnO_x$ microjets at different H_2O_2 concentrations (n=5, error bars represent the standard error of the mean) and C) Swimming trajectories of $SiMnO_x$ and $FeSiMnO_x$ microjets at 5 wt% H_2O_2.

Table 1. Speed comparison of different micromotors propelled by non-metallic catalysts.

Materials in micromotors	Shape	$[H_2O_2]$ (% wt)	Speed ($\mu m\ s^{-1}$)	Approximate body length s^{-1}	Ref.
PEDOT/MnO_2	Tube	5	200±80	16	35
Fullerene-MnO_2	Tube	5	39±5	---	49
MnO_2	Amorphous	12	~50	10	50
Graphene/MnO_2	Tube	5	210.4±80.4	21	51
Graphene/MnO_2	Alveolate	2.5	47.92	7.4	52
PEDOT/MnO_2	tube	6	~125	15.6	53
MOF/Co	Amorphous	5	~25	5	54
MOF/Mn	Amorphous	5	~12	2.4	55
$MnFe_2O_4$	Hollow sphere	2	~260	11	30
$Fe_2O_3/SiO_2/MnO_2$	Tube	5	380.8±38.7	22.4	This work

The presence of γ-Fe_2O_3 NPs provides magnetic properties to the $FeSiMnO_x$ microjets. Taking into account the intended use of microjets for water cleaning, magnetic properties add beneficial functionality for guiding their swimming direction and for their removal by an external magnet after the cleaning treatment,[13,56] avoiding further water contamination by the catalyst itself, which is one the key issues in water treatment.[8] Moreover, the magnetic properties of $FeSiMnO_x$ would

allow to magnetically guide them towards polluted areas that are difficult to access. More importantly, once the different kind of pollutants are removed, the microjets could be guided[13] or transferred[56] to another container for further decontamination processes. **Figure 4A-B** displays the snapshots of the microjets without and with magnetic control, respectively. The orientation of the microjets was randomly distributed in the absence of a magnetic field (**Figure 4C**). After applying the magnetic field, most of the microjets were aligned and following the instructed direction (downward), even in the presence of massive bubbling (**Figure 4D, Video S5)**. As can be seen from **Figures 4E**, after applying the magnetic field, the direction of $FeSiMnO_x$ microjets can be also changed instantly from left to right (**Figure 4E, Video S6**).

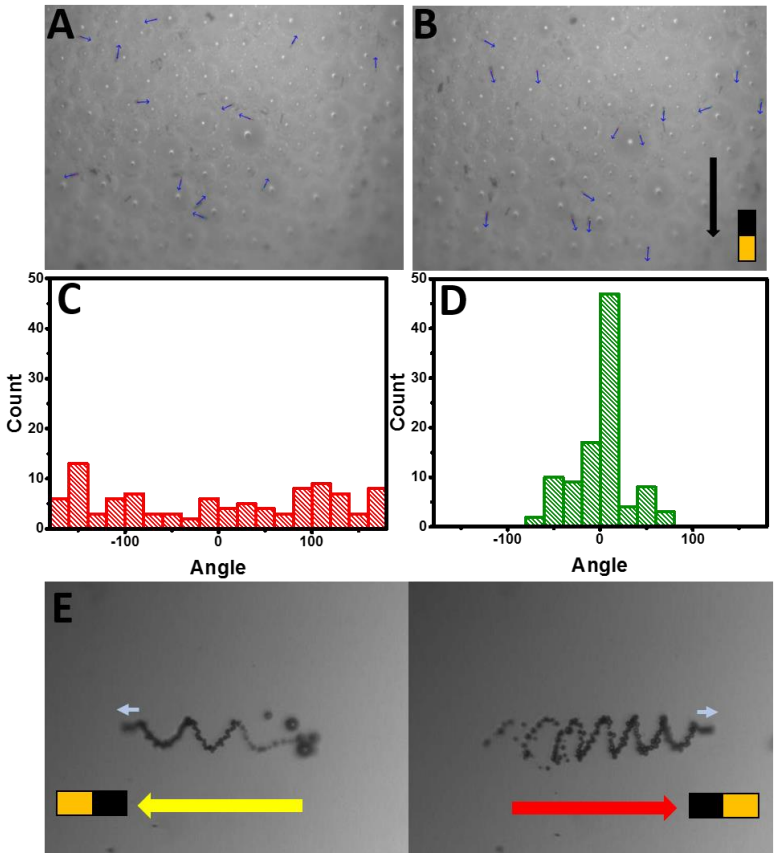

Figure 4. Magnetic control of $FeSiMnO_x$ microjets. A) A snapshot from a video of $FeSiMnO_x$ microjets swimming with random orientation, B) A snapshot from a video of $FeSiMnO_x$ microjets with their orientation controlled by magnetic guidance (downward), C) Distribution of orientation of micromotors without magnetic field (n=100), D) Distribution of orientation of micromotors in the presence of magnetic field along Y axis (n=100) and E) Optical snapshot from a video of $FeSiMnO_x$ microjets controlled by magnetic guidance (left and right).

The photocatalytic performance of the $FeSiMnO_x$ microjets was evaluated upon the degradation of TC and RB (chosen as model pollutants from the pharmaceutical and dye industries, respectively). These kinds of pollutants are known as refractory organic compounds, being very difficult to remove by the classical wastewater treatments. Thus, the design of novel catalytic systems is essential for the efficient degradation of these refractory pollutants.

Firstly, to evaluate the photocatalytic performance of $FeSiMnO_x$ microjets, control experiments without microjets were carried out. To this end, the contribution of H_2O_2 (in the dark) and H_2O_2 plus visible irradiation was studied in the degradation of the above-mentioned pollutants. As can be seen in **Figures 5A-B**, both controls are only degrading 10% and 30% of TC and RB, respectively, after 15 min of treatment. In addition, enhanced degradation rates of both pollutants were not observed after visible irradiation in the presence of H_2O_2 and without micromotors.

The photocatalytic experiments were then performed in the presence of microjets. As it is observed in **Figure 5A** and **5B**, the degradation rates were markedly improved in comparison with the control tests, following an increasing trend: $FeSiMnO_x$ > $SiMnO_x$ > $FeSiMnO_x$ (in the dark) > $FeSiO_x$ microtubes. Since $FeSiO_x$ microtubes (without MnO_2) do not present self-propulsion, the slight degradation performance was due to the photocatalytic properties of Fe_2O_3 NPs on the

surface of $FeSiO_x$ microtubes. In the case of $SiMnO_x$ microjets, MnO_2 can act as a dual catalyst for the decomposition of H_2O_2 to generate O_2 bubbles for the motion but also for the degradation of organic pollutants *via* Fenton-like reaction.[35,57,58] However, as shown in **Figure 5A** and **5B**, the resulting performance is much slower than the one obtained with the $FeSiMnO_x$ microjets.

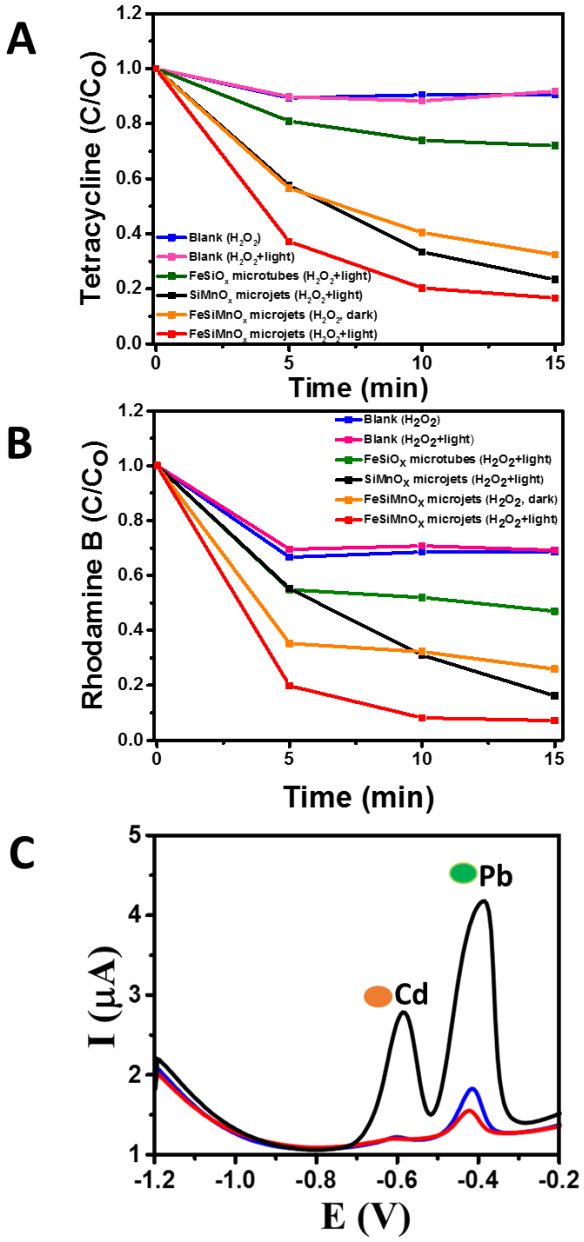

Figure 5. Removal of contaminants in wastewater over $FeSiMnO_x$ microjets after 15 min of reaction. A) C/C_o kinetics of photocatalytic degradation of TC, B) C/C_o kinetics of photocatalytic degradation of RB, C) Removal of lead and cadmium by adsorption on $FeSiMnO_x$ microjets in presence of 10 ppm RB at 0 min (black) after 7 min (blue) and 15 min (red) of reaction.

The fast degradation activity shown by $FeSiMnO_x$ microjets is mainly due to the efficient photocatalytic performance exhibited by γ-Fe_2O_3 NPs on the surface of the microjets, along with the catalytic properties of MnO_2 on the inner surface. When the degradation reactions were carried out in the presence of $FeSiMnO_x$ microjets and H_2O_2 under dark conditions (**Figures 5A and 5B**), the removal yield was much lower than $FeSiMnO_x$ microjets under visible light irradiation.

The mechanism of the photocatalytic degradation of RB and TC involves the activation of γ-Fe_2O_3 photocatalyst with visible irradiation to generate electron-hole pairs. These photogenerated pairs can migrate to the catalyst surface and react with the adsorbed molecules to produce hydroxyl ($HO^{\bullet}$) and superoxide ($O_2^{\bullet -}$) radicals.[59–61] Given the high oxidation potential of these radicals,[62] they can perform the total degradation of the organic matter (pollutants) to non-harmful molecules (CO_2 and water). At the same time, MnO_2 can also produce additional $HO^{\bullet}$ radicals through the Fenton-like reaction in the presence of H_2O_2,[57,63–66] resulting in an enhancement of the total oxidation of the organic pollutants.

Finally, to prove that $FeSiMnO_x$ microjets are capable of removing other types of contaminants, we selected Cd^{2+} and Pb^{2+} as model pollutants of toxic heavy metals. Taking advantage of the interactions between Fe_2O_3 NPs and heavy metals[67,68], we used $FeSiMnO_x$ microjets for the removal of Cd^{2+} and Pb^{2+} in the presence of another pollutant, such as RB. **Figure 5C** illustrates the results corresponding to the capture of both heavy metals after 7 and 15 min of treatment with

0.3 mg $FeSiMnO_x$ microjets in 5% H_2O_2. It was observed that $FeSiMnO_x$ microjets were able to remove more than 98% and 94% (n=3) of Cd^{2+} and Pb^{2+}, respectively, from a contaminated water with 1 ppm of each metal. Thus, we demonstrated that $FeSiMnO_x$ microjets can be used for the efficient remediation of several classes of contaminants, such as antibiotics, dyes and heavy metals in wastewater.

4. CONCLUSIONS

In conclusion, we have developed highly efficient $FeSiMnO_x$ microjets for multifunctional environmental applications, such as the degradation of persistent organic pollutants under visible irradiation and the removal of heavy metals from wastewater. The microjets can be easily guided and extracted using a magnetic field. Remarkably, $FeSiMnO_x$ microjets exhibited the highest speed (485±32 μm s^{-1}) that has been obtained so far for tubular micromotors powered by non-noble metals such as MnO_2. The synthesis of microjets was carried out using only chemical methods and simple apparatus, which is an advantage for their eventual mass-production. The strategy of combining two metal oxides (Fe_2O_3/MnO_2) that are able to decompose H_2O_2 with simultaneous generation of hydroxyl radicals resulted in a significant improvement in the photocatalytic performance of the microjets. This approach opens up new inexpensive alternative methods to fabricate other types of metal-oxide based microjets and microtubular structures for different applications in the environmental field.

ASSOCIATED CONTENT

Supporting Information.

The following files are available free of charge.

Figure S1. TEM EDX-Mapping images of different $SiMnO_x$ microjets (file type, Word)

Figure S2. SEM characterization of $SiMnO_x$ microjets synthesized with different $KMnO_4$ concentrations (file type, Word)

Video S1. Motion of $SiMnO_x$ microjets (20 mM $KMnO_4$).

Video S2. Motion of $SiMnO_x$ microjets (30 mM $KMnO_4$).

Video S3. Motion of $SiMnO_x$ microjets.

Video S4. Motion of $FeSiMnO_x$ microjets.

Video S5. Magnetic control (downward direction).

Video S6. Magnetic control (left and right direction).

AUTHOR INFORMATION

Corresponding Author

* Phone: +34 934 020 558; email: ssanchez@ibecbarcelona.eu

Author Contributions

The manuscript was written through contributions of all authors. All authors have given approval to the final version of the manuscript.

£ These authors contributed equally.

Acknowledgments

The research leading to these results has received funding from the European Research Council under the European Union's Seventh Framework Program (FP7/20072013)/ERC grant agreement no. 311529 (LT-NRBS) and ERC-2015-PoC/Project ID: 713608 (MICROCLEANERS). S.S. thanks the Spanish MINECO for grants CTQ2015-68879-R (MICRODIA). D. V. acknowledges

financial support provided by the European Commission under Horizon 2020's Marie Skłodowska-Curie Actions COFUND scheme [Grant Agreement No. 712754] and by the Severo Ochoa programme of the Spanish Ministry of Economy and Competitiveness [Grant SEV-2014-0425 (2015–2019)]. IBEC group thanks the CERCA Programme / Generalitat de Catalunya. The authors thank the Stuttgart Center for Electron Microscopy (StEM) and the support of Mr. Kersten Hahn in the TEM and EELS investigations. The authors thank A. Miguel-López for the development of the magnetic control setup and the Python-based software for the tracking of micromotors.

REFERENCES

(1) Kumar Gupta, V.; Ali, I.; A. Saleh, T.; Nayak, A.; Agarwal, S. Chemical Treatment Technologies for Waste-Water Recycling—an Overview. *RSC Adv.* **2012**, *2* (16), 6380–6388.
(2) Chong, M. N.; Jin, B.; Chow, C. W. K.; Saint, C. Recent Developments in Photocatalytic Water Treatment Technology: A Review. *Water Res.* **2010**, *44* (10), 2997–3027.
(3) Shannon, M. A.; Bohn, P. W.; Elimelech, M.; Georgiadis, J. G.; Marinas, B. J.; Mayes, A. M. Science and Technology for Water Purification in the Coming Decades. *Nature* **2008**, *452* (7185), 301–310.
(4) Qu, X.; Brame, J.; Li, Q.; Alvarez, P. J. J. Nanotechnology for a Safe and Sustainable Water Supply: Enabling Integrated Water Treatment and Reuse. *Acc. Chem. Res.* **2013**, *46* (3), 834–843.
(5) Soler, L.; Sánchez, S. Catalytic Nanomotors for Environmental Monitoring and Water Remediation. *Nanoscale* **2014**, *6* (13), 7175–7182.
(6) Gao, W.; Wang, J. The Environmental Impact of Micro/Nanomachines: A Review. *Acs Nano* **2014**, *8* (4), 3170–3180.
(7) Safdar, M.; Simmchen, J.; Jänis, J. Light-Driven Micro- and Nanomotors for Environmental Remediation. *Environ. Sci. Nano* **2017**, *4* (8), 1602–1616.
(8) Moo, J. G. S.; Pumera, M. Chemical Energy Powered Nano/Micro/Macromotors and the Environment. *Chem. – Eur. J.* **2015**, *21* (1), 58–72.
(9) Katuri, J.; Ma, X.; Stanton, M. M.; Sánchez, S. Designing Micro- and Nanoswimmers for Specific Applications. *Acc. Chem. Res.* **2017**, *50* (1), 2–11.
(10) Guix, M.; Orozco, J.; García, M.; Gao, W.; Sattayasamitsathit, S.; Merkoçi, A.; Escarpa, A.; Wang, J. Superhydrophobic Alkanethiol-Coated Microsubmarines for Effective Removal of Oil. *ACS Nano* **2012**, *6* (5), 4445–4451.
(11) Soler, L.; Magdanz, V.; Fomin, V. M.; Sanchez, S.; Schmidt, O. G. Self-Propelled Micromotors for Cleaning Polluted Water. *ACS Nano* **2013**, *7* (11), 9611–9620.

(12) Lin Zhihua; Wu Zhiguang; Lin Xiankun; He Qiang. Catalytic Polymer Multilayer Shell Motors for Separation of Organics. *Chem. – Eur. J.* **2015**, *22* (5), 1587–1591.
(13) Vilela, D.; Parmar, J.; Zeng, Y.; Zhao, Y.; Sánchez, S. Graphene-Based Microbots for Toxic Heavy Metal Removal and Recovery from Water. *Nano Lett.* **2016**, *16* (4), 2860–2866.
(14) Uygun, D. A.; Jurado-Sánchez, B.; Uygun, M.; Wang, J. Self-Propelled Chelation Platforms for Efficient Removal of Toxic Metals. *Environ. Sci. Nano* **2016**, *3* (3), 559–566.
(15) Vilela, D.; Stanton, M. M.; Parmar, J.; Sánchez, S. Microbots Decorated with Silver Nanoparticles Kill Bacteria in Aqueous Media. *ACS Appl. Mater. Interfaces* **2017**.
(16) Ge, Y.; Liu, M.; Liu, L.; Sun, Y.; Zhang, H.; Dong, B. Dual-Fuel-Driven Bactericidal Micromotor. *Nano-Micro Lett.* **2016**, *8* (2), 157–164.
(17) Li, J.; Singh, V. V.; Sattayasamitsathit, S.; Orozco, J.; Kaufmann, K.; Dong, R.; Gao, W.; Jurado-Sanchez, B.; Fedorak, Y.; Wang, J. Water-Driven Micromotors for Rapid Photocatalytic Degradation of Biological and Chemical Warfare Agents. *ACS Nano* **2014**, *8* (11), 11118–11125.
(18) Howse, J. R.; Jones, R. A. L.; Ryan, A. J.; Gough, T.; Vafabakhsh, R.; Golestanian, R. Self-Motile Colloidal Particles: From Directed Propulsion to Random Walk. *Phys. Rev. Lett.* **2007**, *99* (4), 048102.
(19) Gao, W.; Pei, A.; Dong, R.; Wang, J. Catalytic Iridium-Based Janus Micromotors Powered by Ultralow Levels of Chemical Fuels. *J. Am. Chem. Soc.* **2014**, *136* (6), 2276–2279.
(20) Wang, H.; Sofer, Z.; Eng, A. Y. S.; Pumera, M. Iridium-Catalyst-Based Autonomous Bubble-Propelled Graphene Micromotors with Ultralow Catalyst Loading. *Chem. – Eur. J.* **2014**, *20* (46), 14946–14950.
(21) Paxton, W. F.; Kistler, K. C.; Olmeda, C. C.; Sen, A.; St. Angelo, S. K.; Cao, Y.; Mallouk, T. E.; Lammert, P. E.; Crespi, V. H. Catalytic Nanomotors: Autonomous Movement of Striped Nanorods. *J. Am. Chem. Soc.* **2004**, *126* (41), 13424–13431.
(22) Xuan Mingjun; Lin Xiankun; Shao Jingxin; Dai Luru; He Qiang. Motion-Based, High-Yielding, and Fast Separation of Different Charged Organics in Water. *ChemPhysChem* **2014**, *16* (1), 147–151.
(23) Gao, W.; Sattayasamitsathit, S.; Orozco, J.; Wang, J. Highly Efficient Catalytic Microengines: Template Electrosynthesis of Polyaniline/Platinum Microtubes. *J. Am. Chem. Soc.* **2011**, *133* (31), 11862–11864.
(24) Wu, Z.; Wu, Y.; He, W.; Lin, X.; Sun, J.; He, Q. Self-Propelled Polymer-Based Multilayer Nanorockets for Transportation and Drug Release. *Angew. Chem. Int. Ed.* **2013**, *52* (27), 7000–7003.
(25) Wu, Z.; Lin, X.; Wu, Y.; Si, T.; Sun, J.; He, Q. Near-Infrared Light-Triggered "on/off" Motion of Polymer Multilayer Rockets. *Acs Nano* **2014**, *8* (6), 6097–6105.
(26) Mei, Y.; Huang, G.; Solovev, A. A.; Ureña, E. B.; Mönch, I.; Ding, F.; Reindl, T.; Fu, R. K. Y.; Chu, P. K.; Schmidt, O. G. Versatile Approach for Integrative and Functionalized Tubes by Strain Engineering of Nanomembranes on Polymers. *Adv. Mater.* **2008**, *20* (21), 4085–4090.
(27) Parmar, J.; Ma, X.; Katuri, J.; Simmchen, J.; Stanton, M. M.; Carolina Trichet-Paredes; Soler, L.; Sanchez, S. Nano and Micro Architectures for Self-Propelled Motors. *Sci. Technol. Adv. Mater.* **2015**, *16* (1), 014802.
(28) Maric, T.; Moo, J. G. S.; Khezri, B.; Sofer, Z.; Pumera, M. Black-Phosphorus-Enhanced Bubble-Propelled Autonomous Catalytic Microjets. *Appl. Mater. Today* **2017**, *9*, 289–291.

(29) Wang, H.; Pumera, M. Fabrication of Micro/Nanoscale Motors. *Chem. Rev.* **2015**, *115* (16), 8704–8735.
(30) Mou, F.; Pan, D.; Chen, C.; Gao, Y.; Xu, L.; Guan, J. Magnetically Modulated Pot-Like MnFe2O4 Micromotors: Nanoparticle Assembly Fabrication and Their Capability for Direct Oil Removal. *Adv. Funct. Mater.* **2015**, *25* (39), 6173–6181.
(31) Wang, L.; Liu, Y.; He, J.; Hourwitz, M. J.; Yang, Y.; Fourkas, J. T.; Han, X.; Nie, Z. Continuous Microfluidic Self-Assembly of Hybrid Janus-Like Vesicular Motors: Autonomous Propulsion and Controlled Release. *Small* **2015**, *11* (31), 3762–3767.
(32) Seo, K. D.; Kwak, B. K.; Sánchez*, S.; Kim*, D. S. Microfluidic-Assisted Fabrication of Flexible and Location Traceable Organo-Motor. *IEEE Trans. NanoBioscience* **2015**, *14* (3), 298–304.
(33) Parmar, J.; Villa, K.; Vilela, D.; Sánchez, S. Platinum-Free Cobalt Ferrite Based Micromotors for Antibiotic Removal. *Appl. Mater. Today* **2017**, *9* (Supplement C), 605–611.
(34) Vilela, D.; Hortelao, A. C.; Balderas-Xicohténcatl, R.; Hirscher, M.; Hahn, K.; Ma, X.; Sánchez, S. Facile Fabrication of Mesoporous Silica Micro-Jets with Multi-Functionalities. *Nanoscale* **2017**, *9* (37), 13990–13997.
(35) Safdar, M.; Wani, O. M.; Jänis, J. Manganese Oxide-Based Chemically Powered Micromotors. *ACS Appl. Mater. Interfaces* **2015**, *7* (46), 25580–25585.
(36) Zhao, G.; Sanchez, S.; Schmidt, O. G.; Pumera, M. Poisoning of Bubble Propelled Catalytic Micromotors: The Chemical Environment Matters. *Nanoscale* **2013**, *5* (7), 2909–2914.
(37) Minh, T. D.; Safdar, M.; Jänis, J. Protection of Platinum-Based Micromotors from Thiol Toxicity by Using Manganese Oxide. *Chem. – Eur. J.* **2017**, *23* (34), 8134–8136.
(38) Teo, W. Z.; Wang, H.; Pumera, M. Beyond Platinum: Silver-Catalyst Based Bubble-Propelled Tubular Micromotors. *Chem. Commun.* **2016**, *52* (23), 4333–4336.
(39) Parmar, J.; Vilela, D.; Pellicer, E.; Esqué-de los Ojos, D.; Sort, J.; Sánchez, S. Reusable and Long-Lasting Active Microcleaners for Heterogeneous Water Remediation. *Adv. Funct. Mater.* **2016**, *26* (23), 4152–4161.
(40) Mushtaq, F.; Guerrero, M.; Sakar, M. S.; Hoop, M.; Lindo, A. M.; Sort, J.; Chen, X.; Nelson, B. J.; Pellicer, E.; Pane, S. Magnetically Driven Bi2O3/BiOCl-Based Hybrid Microrobots for Photocatalytic Water Remediation. *J. Mater. Chem. A* **2015**, *3* (47), 23670–23676.
(41) Zhang, Q.; Dong, R.; Wu, Y.; Gao, W.; He, Z.; Ren, B. Light-Driven Au-WO3@C Janus Micromotors for Rapid Photodegradation of Dye Pollutants. *ACS Appl. Mater. Interfaces* **2017**, *9* (5), 4674–4683.
(42) Villa, K.; Domènech, X.; García-Pérez, U. M.; Peral, J. Optimization of the Experimental Conditions of Hydrogen Production by the Pt–(CdS/ZnS) System under Visible Light Illumination. *RSC Adv.* **2016**, *6* (43), 36681–36688.
(43) Bahnemann, D. Photocatalytic Water Treatment: Solar Energy Applications. *Sol. Energy* **2004**, *77* (5), 445–459.
(44) Villa, K.; Domènech, X.; García-Pérez, U. M.; Peral, J. Photocatalytic Hydrogen Production Under Visible Light by Using a CdS/WO3 Composite. *Catal. Lett.* **2016**, *146* (1), 100–108.
(45) Kopf, R. F. *State-of-the-Art Program on Compound Semiconductors XXXIX and Nitride and Wide Bandgap Semiconductors for Sensors, Photonics and Electronics IV: Proceedings of the International Symposia*; The Electrochemical Society, 2003.
(46) Wang, J.; Tian, B. Screen-Printed Stripping Voltammetric/Potentiometric Electrodes for Decentralized Testing of Trace Lead. *Anal. Chem.* **1992**, *64* (15), 1706–1709.

(47) Lin, S.-S.; Gurol, M. D. Catalytic Decomposition of Hydrogen Peroxide on Iron Oxide: Kinetics, Mechanism, and Implications. *Environ. Sci. Technol.* **1998**, *32* (10), 1417–1423.
(48) Hermanek, M.; Zboril, R.; Medrik, I.; Pechousek, J.; Gregor, C. Catalytic Efficiency of Iron(III) Oxides in Decomposition of Hydrogen Peroxide: Competition between the Surface Area and Crystallinity of Nanoparticles. *J. Am. Chem. Soc.* **2007**, *129* (35), 10929–10936.
(49) Huang, H.-H.; Lu, M.-C.; Chen, J.-N. Catalytic Decomposition of Hydrogen Peroxide and 2-Chlorophenol with Iron Oxides. *Water Res.* **2001**, *35* (9), 2291–2299.
(50) Maria-Hormigos, R.; Jurado-Sanchez, B.; Vazquez, L.; Escarpa, A. Carbon Allotrope Nanomaterials Based Catalytic Micromotors. *Chem. Mater.* **2016**, *28* (24), 8962–8970.
(51) Wang, H.; Zhao, G.; Pumera, M. Beyond Platinum: Bubble-Propelled Micromotors Based on Ag and MnO2 Catalysts. *J. Am. Chem. Soc.* **2014**, *136* (7), 2719–2722.
(52) Ye, H.; Sun, H.; Wang, S. Electrochemical Synthesis of Graphene/MnO2 in an Architecture of Bilayer Microtubes as Micromotors. *Chem. Eng. J.* **2017**, *324*, 251–258.
(53) Feng, X.; Zhang, Y.; Li, Y.; Huang, Z.; Chen, S.; Ma, Y.; Zhang, L.; Wang, L.; Yan, X. Graphene-Based Highly Efficient Micromotors. *Chem. Lett.* **2014**, *44* (3), 399–401.
(54) Singh, A. K.; Mandal, T. K.; Bandyopadhyay, D. Magnetically Guided Chemical Locomotion of Self-Propelling Paperbots. *RSC Adv.* **2015**, *5* (79), 64444–64449.
(55) Wang, L.; Chen, J.; Feng, X.; Zeng, W.; Liu, R.; Lin, X.; Ma, Y.; Wang, L. Self-Propelled Manganese Oxide-Based Catalytic Micromotors for Drug Delivery. *RSC Adv.* **2016**, *6* (70), 65624–65630.
(56) Li, J.; Yu, X.; Xu, M.; Liu, W.; Sandraz, E.; Lan, H.; Wang, J.; Cohen, S. M. Metal–Organic Frameworks as Micromotors with Tunable Engines and Brakes. *J. Am. Chem. Soc.* **2017**, *139* (2), 611–614.
(57) Kim, E.-J.; Oh, D.; Lee, C.-S.; Gong, J.; Kim, J.; Chang, Y.-S. Manganese Oxide Nanorods as a Robust Fenton-like Catalyst at Neutral PH: Crystal Phase-Dependent Behavior. *Catal. Today* **2017**, *282*, 71–76.
(58) Valim, R. B.; Santos, M. C.; Lanza, M. R. V.; Machado, S. A. S.; Lima, F. H. B.; Calegaro, M. L. Oxygen Reduction Reaction Catalyzed by Ɛ-MnO2: Influence of the Crystalline Structure on the Reaction Mechanism. *Electrochimica Acta* **2012**, *85*, 423–431.
(59) Saghi, M.; Mahanpoor, K. Photocatalytic Degradation of Tetracycline Aqueous Solutions by Nanospherical α-Fe<Subscript>2</Subscript>O<Subscript>3</Subscript> Supported on 12-Tungstosilicic Acid as Catalyst: Using Full Factorial Experimental Design. *Int. J. Ind. Chem.* **2017**, *8* (3), 297–313.
(60) Li, R.; Jia, Y.; Wu, J.; Zhen, Q. Photocatalytic Degradation and Pathway of Oxytetracycline in Aqueous Solution by Fe2O3–TiO2 Nanopowder. *RSC Adv.* **2015**, *5* (51), 40764–40771.
(61) Mahamallik, P.; Saha, S.; Pal, A. Tetracycline Degradation in Aquatic Environment by Highly Porous MnO2 Nanosheet Assembly. *Chem. Eng. J.* **2015**, *276* (Supplement C), 155–165.
(62) Villa, K.; Murcia-López, S.; Andreu, T.; Morante, J. R. On the Role of WO3 Surface Hydroxyl Groups for the Photocatalytic Partial Oxidation of Methane to Methanol. *Catal. Commun.* **2015**, *58* (Supplement C), 200–203.
(63) Fei, J. B.; Cui, Y.; Yan, X. H.; Qi, W.; Yang, Y.; Wang, K. W.; He, Q.; Li, J. B. Controlled Preparation of MnO2 Hierarchical Hollow Nanostructures and Their Application in Water Treatment. *Adv. Mater.* **2008**, *20* (3), 452–456.
(64) Zbiljić, J.; Guzsvány, V.; Vajdle, O.; Prlina, B.; Agbaba, J.; Dalmacija, B.; Kónya, Z.; Kalcher, K. Determination of H2O2 by MnO2 Modified Screen Printed Carbon Electrode

during Fenton and Visible Light-Assisted Photo-Fenton Based Removal of Acetamiprid from Water. *J. Electroanal. Chem.* **2015**, *755* (Supplement C), 77–86.

(65) Zhang, Y.; Liu, C.; Xu, B.; Qi, F.; Chu, W. Degradation of Benzotriazole by a Novel Fenton-like Reaction with Mesoporous Cu/MnO2: Combination of Adsorption and Catalysis Oxidation. *Appl. Catal. B Environ.* **2016**, *199* (Supplement C), 447–457.

(66) Villa, K.; Parmar, J.; Vilela, D.; Sánchez, S. Core–shell Microspheres for the Ultrafast Degradation of Estrogen Hormone at Neutral PH. *RSC Adv.* **2018**, *8* (11), 5840–5847.

(67) Cao, C.-Y.; Qu, J.; Yan, W.-S.; Zhu, J.-F.; Wu, Z.-Y.; Song, W.-G. Low-Cost Synthesis of Flowerlike α-Fe2O3 Nanostructures for Heavy Metal Ion Removal: Adsorption Property and Mechanism. *Langmuir* **2012**, *28* (9), 4573–4579.

(68) Hu, J.-S.; Zhong, L.-S.; Song, W.-G.; Wan, L.-J. Synthesis of Hierarchically Structured Metal Oxides and Their Application in Heavy Metal Ion Removal. *Adv. Mater.* **2008**, *20* (15), 2977–2982.